

# Flexible quasi-2D inversion of time-domain AEM data, using a wavelet-based complexity measure

Wouter Deleersnyder<sup>1,2</sup>, Benjamin Maveau<sup>1</sup>, David Dudal<sup>1,3</sup>, Thomas Hermans<sup>2</sup>,

<sup>1</sup>KU Leuven Campus Kortrijk - KULAK, Department of Physics, Etienne Sabbelaan 53, 8500 Kortrijk, Belgium.

E-mail: wouter.deleersnyder@kuleuven.be

<sup>2</sup>Ghent University, Department of Geology, Krijgslaan 281 - S8, 9000 Gent, Belgium

<sup>3</sup>Ghent University, Department of Physics and Astronomy, Ghent, Krijgslaan 281 - S9, 9000 Gent, Belgium

## ABSTRACT

Regularization methods improve the stability of ill-posed inverse problems by introducing some a priori characteristics for the solution such as smoothness or sharpness. In this contribution, we propose a multidimensional, scale-dependent wavelet-based  $\ell_1$ -regularization term to cure the ill-posedness of the airborne (time-domain) electromagnetic induction inverse problem. The regularization term is flexible, as it can recover blocky, smooth and tunable in-between inversion models, based on a suitable wavelet basis function. For each orientation, a different wavelet basis function can be used, introducing an additional relative regularization parameter. We propose a calibration method to determine (an educated initial guess for) this relative regularization parameter, which reduces the need to optimize for this parameter, and, consequently, the overall computation time is under control. We apply our novel scheme to a time-domain airborne electromagnetic data set in Belgian saltwater intrusion context, but the scheme could equally apply to any other 2D or 3D geophysical inverse problem.

Keywords: Inverse theory – Wavelet transform – Electromagnetic theory – Controlled source electromagnetics (CSEM)

**Submitted to Geophysical Journal International**

## 1 INTRODUCTION

The Airborne ElectroMagnetic induction (AEM) method is a practical tool to map near-surface geological features over large areas (a few tens of kilometres) via the bulk electrical resistivity. It is increasingly used for mineral exploration (Macnae and Milkereit, 2007), hydrogeological mapping (Mikucki et al., 2015; Podgorski et al., 2013), saltwater intrusion (Goebel et al., 2019; Siemon et al., 2019) and contamination (Pfaffhuber et al., 2017). The focus in AEM is mainly on (dual moment) time-domain systems, as they allow for an improved near-surface resolution and an increased depth of penetration. While the AEM systems have massively advanced within the last decades (Auken et al., 2017), there are two main impediments in the data interpretation process, which are also a concern for other electromagnetic geophysical methods. The first difficulty is the computational burden related to the computation of the forward model, which describes the soil's response to a specific subsurface realization and specific survey set-up. To date, most inversion schemes use a one dimensional model, which assume horizontal layers without lateral variations. The second challenge lies in the fact that geophysical inversion (in general) is an ill-posed problem, meaning that the solution is typically not unique. This is usually dealt with via regularization techniques.

Deterministic regularization techniques impose one or more constraints on the model parameters or inversion model. It is generally a minimum-structure inversion, meaning that unrealistic electrical conductivities are filtered out and the “simplest” inversion model is promoted. “Simple” means that we

aim for the model with the least number of features that explains the data equally well as other more exciting models with more (potentially attractive) features. This is Occam's inversion approach articulated by Constable et al. (1987), who popularised smoothness based regularization for electromagnetic sounding data. The smoothness constraint, such as the traditional Tikhonov regularization (Tikhonov, 1943) or more recent Laterally Constrained Inversion (LCI) (Auken and Christiansen, 2004), is not always adapted to the subsurface structure (Linde et al., 2015). Smoothness regularization improves the stability of the inversion, however, too much regularization smears out small-scale features, while little regularization reduces the stability. Moreover, blocky structures or sharp interfaces cannot be recovered. While many alternative minimum-structure schemes exist, it is not always easy to find the best adapted scheme. One flexible inversion scheme supporting multiple types of minimum-structure constraints could simplify the generation of an ensemble of various inversion models.

Quasi-2D inversion schemes produce realistic 2D inversion models by imposing regularization conditions in both dimensions. In contrast to 2D inversion schemes, these schemes rely on 1D forward modelling due to the computational burden of accurate 2.5D or 3D modelling. Common 2D regularization schemes use smoothing, minimization of the total variation or wavelet theory. A traditional method for minimum structure inversion is to apply a smoothing constraint, such as with Tikhonov regularization along all the orientations (Tikhonov, 1943). Tikhonov regularization promotes smooth solutions and hence cannot recover blocky structures. Laterally Constrained Inversion (LCI) (Auken and Christiansen, 2004) is capable of producing laterally smooth transitions by adding roughening constraints to the objective function that tie model parameters of adjacent layers. Via a roughening matrix, the dissimilarity between neighbouring cells is measured and minimized in combination with a data misfit. Amongst its successors are Spatially Constrained Inversion (SCI) for smooth quasi-3D inversion by Viezzoli et al. (2008) and sharp SCI, which favours more blocky models (Vignoli et al., 2015; Klose et al., 2022). Another similar approach is the lateral parameter correlation (LPC) (Christensen, 2016). This approach firstly inverts the data without constraints. Then, a laterally smooth version of the inversion model is generated. The method finishes with a final inversion on a starting model which is a result of a covariance analysis of the constrained and unconstrained inversion model. Total variation regularization methods with several focusing functions are mostly sparsity-based, such as the  $\ell_1$ -norm, and successfully recover blocky structures (Farquharson, 2007). Other examples are the minimum gradient support functional (Thibaut et al., 2021) or a sequential inversion (Guillemoteau et al., 2016). There are many alternatives such as covariance-based inversion (Hermans et al., 2012; Paasche and Tronicke, 2007). Recently, (sparsity-based) wavelet-based regularization schemes have been applied to geophysical inversion. Nittinger and Becken (2016) present a 2D, wavelet-based sparsity inversion scheme for magnetotelluric data based on Daubechies et al. (2004)'s work on the iterative soft thresholding algorithm for solving objective functions with both an  $\ell_1$  and  $\ell_2$ -norm. A particular complex dual-tree wavelet representation, yielding six directions of a smooth shape, is utilised. Liu et al. (2017) apply a 3D wavelet-based method to frequency AEM data and compares the effect of various wavelet basis functions to the inversion result. Liu et al. (2017) conclude that smooth wavelet basis functions produce more stable results. Nittinger and Becken (2018) already report an advantageous feature of wavelet-based inversion, that of the simultaneous occurrence of smooth and sharp anomalies within the same model. In our earlier work (Deleersnyder et al., 2021), this observation is confirmed with a novel scale-dependent wavelet-based regularization scheme for 1D geophysical inversion. The scale-dependency produces stable inversion models for all the common wavelet basis functions (also the blocky and irregular-shaped basis functions), which leads to a more flexible inversion scheme (as it can recover both blocky, intermediate and smooth profiles). All the 2D inversion schemes listed above are most successful with the inversion of either blocky or smooth results, but fail to generate an ensemble of inversion models with different features with the ease of changing a simple tuning parameter. In this work, the flexible scheme of Deleersnyder et al. (2021) is extended into two dimensions. The generalization of the scale-dependent scheme comes with a few challenges and design preferences, which are described below.

The regularization scheme in this work differs from the other 2/3D wavelet-based methods first and foremost because of the implementation of scale-dependency of the complexity measure proposed in Deleersnyder et al. (2021) for 1D inversion. Additionally, we consider a complexity measure per orientation. This allows imposing a different type of structure (blocky, smooth, ...) on the inversion model for each orientation. Due to this design choice, we can no longer optimize the inverse problem in the

wavelet domain (as in our earlier work). First, we would have (at least) twice as many parameters to optimize as in model space, which makes the inverse problem more computationally expensive. Secondly, the recovered inversion model in the wavelet domain would be difficult to consistently back transform to the model space. Therefore, in this work, the inverse problem is solved in model space instead, by making use of the chain rule. There can be no inconsistency because there is no redundancy in the optimization parameters. The optimization problem in the model domain does not complicate our previously developed regularization scheme and does not require modifications to the scheme due to this rationale. In 2D wavelet-based regularization, a growing body of literature focuses on (multi)directionality: how do we recover diagonal features? As previously mentioned, Nittinger and Becken (2016) therefore specifically uses a 2D wavelet with six directions. In recent work (Su et al., 2021), the shearlet transform is utilised. This is an extension of the wavelet transform that is supplemented with some notion of directionality. This gives rise to an even higher redundancy: A 64x64 inversion model requires a representation of 606 208 shearlet coefficients on which the sparsity condition is imposed (a priori unknown indices). Moreover, we believe that the standard 2D wavelet transform has a disadvantage in 2D inversion because with more symmetric basis functions it will also generate more symmetric inversion models. By introducing a separate complexity measure for each direction, we do not implicitly imply such a symmetry. Our findings are that we do not experience any problems with directionality, certainly not so that they complicate the geological interpretation.

Another advantage of our approach is that no square inversion models are required, which is certainly welcome for AEM inversion where the number of soundings along a profile is typically much bigger than the number of model parameters in the vertical orientation. In other wavelet-based methods, where for example an inversion model with shape of 30 by 64 would be ideal, it should be extended to a 64x64 inversion model in order to apply the 2D discrete wavelet transform, which in turn affects the computation time of the Jacobian of the data-fitting term.

The separation of the complexity measure into an individual complexity measure for each orientation introduces an additional relative weighting parameter. To tackle this, we introduce a calibration step that we can deploy prior to the 2D inversion and yield an estimate for that relative weighting parameter. This calibration step is based on heuristics and uses the variation in the EM field data as an estimate for the lateral complexity. This calibration step is further described in Section 2.2.5. In Section 3, a synthetic model and field data case in a salinization context is presented. The field AEM data is from Flanders Environment Agency (Delsmans et al., 2019) and is the basis of Flanders' current salinization map, showing the depth of the fresh-saltwater interface.

## 2 METHODS

### 2.1 The objective function

Due to the non-linearity of accurate time-domain electromagnetic (TDEM) forward operators, the inverse problem is solved iteratively as an optimization problem, where an objective function is minimized. The objective function  $\phi$  takes the model parameters  $\mathbf{M}$  (the electrical conductivities) as input and expresses how well those parameters fit the data. In minimum structure inversion procedures, an additional measure of model complexity (also known as regularization or model misfit term) is added to the objective function in order to stabilize the inverse problem. The minimum of the objective function  $\phi$  is usually obtained via gradient based methods (see Section 2.4). In general, the objective function for a geophysical inversion problem is

$$\phi(\mathbf{M}) = \phi_d + \beta \phi_m, \quad (1)$$

where  $\phi_d$  and  $\phi_m$  are the data misfit and model misfit, respectively.  $\beta$  is a regularization parameter (also called trade-off parameter) which balances the relative importance of the two misfits. When the regularization parameter  $\beta$  is too small, the optimization algorithm will be over-fitting the data and the geological interpretation of the inversion model is problematic. Too large regularization parameters yield too simple inversion models.

The data misfit functional  $\phi_d$  measures how well the model parameters  $\mathbf{M}$  fit the data. In our inversion

scheme, we use the traditional weighted least-squares data-fitting term or chi-square misfit function

$$\phi_d = \frac{1}{n_d} \|\mathbf{W}_d (\mathbf{d} - \mathcal{F}(\mathbf{M}))\|_2^2, \quad (2)$$

where  $n_d$  is the number of data points, the vector  $\mathbf{d} \in \mathbb{R}^{n_d}$  contains the observed data of the AEM survey and  $\mathcal{F}(\mathbf{M})$  is the predicted data via the forward model  $\mathcal{F}$  (see Section 2.3). The diagonal matrix  $\mathbf{W}_d$  contains the reciprocals of the estimated noise standard deviation. LaBrecque et al. (1996) showed that a correct estimation of the noise floor and standard deviation is crucial. As AEM data span multiple orders of magnitude, the percent uncertainty is especially important, it prevents over-fitting the large values at the expense of under-fitting the small data values. From statistical theory, the chi-square criterion can be adopted (Kemna, 2000), meaning that a good inversion model fits the data within the noise level and that the data misfit  $\phi_d$  (or error weighted root mean-squared error  $\epsilon_{\text{RMS}} = \sqrt{\phi_d}$ ) is close to 1.

The model misfit functional  $\phi_m$  imposes the additional constraints on the inversion model in an Occam's sense and handles the ill-posedness of the problem. In contrast to parametric models, voxel-based models typically contain much more model parameters and consequently the solution is not unique. In the next section, our multidimensional scale-dependent wavelet-based complexity measure is introduced.

## 2.2 Scale-dependent wavelet-based complexity measure

In this section, we extend the work of Deleersnyder et al. (2021) into two dimensions. We provide a more visual and intuitive description of the method and highlight the differences with the one dimensional model misfit. For a more mathematical background about wavelet theory or specific details that remain unchanged with respect to the 1D model misfit, we refer to Deleersnyder et al. (2021).

The 2D scale-dependent wavelet-based regularization term will be described in a step-by-step manner. An inversion model  $\mathbf{M} \in \mathbb{R}^{n_m \times n_s}$  is a matrix, where  $n_m$  is the number of layers and  $n_s$  is the number of soundings, an example with an illustrative discretization is shown in Figure 1A. That inversion model  $\mathbf{M}$  is sliced along both vertical and lateral orientation as 1D layer snippets  $\mathbf{m}$ , as demonstrated in Figure 1B-1C. The model misfit  $\phi_m$  splits into a sum of model misfits per orientation:

$$\phi_m(\mathbf{M}) = \phi_{m,\updownarrow}(\mathbf{M}) + \alpha \phi_{m,\leftrightarrow}(\mathbf{M}), \quad (3)$$

where  $\alpha$  sets the relative importance of those terms.

### 2.2.1 Measuring model complexity with the discrete wavelet transform

Suppose that there exists a basis in which the true model parameters  $\mathbf{M}$ , known to possess minimum structure, are represented in a sparse fashion. Such a basis in combination with a sparsity promoting measure would yield an appropriate model misfit. This would also mean that a randomly generated model (or a heavily over-fitted model that one typically gets by setting the regularization parameter  $\beta$  too low) would also be random in that basis. This would be heavily penalized by the sparsity promoting measure and therefore that  $\mathbf{M}$  would not be a minimum of  $\phi$ .

The discrete wavelet transform can be interpreted as a basis transformation  $\mathbf{W}$  which transforms an inversion model snippet  $\mathbf{m}$  from the model domain into the wavelet domain with coefficients  $x_i$ . The discrete wavelet transform allows to represent the conductivity profile (or horizontal cross-section) in a sparse fashion, because it has both spatial and temporal resolution (the nomenclature temporal stems from the relation to the frequency domain, i.e. width of the signal, while spatial is related to the location of the wavelet basis function). It is intuitive to compare the wavelet transform with the Fourier transform. In Fourier analysis, we represent a signal/model in time/model domain and map it to the frequency domain. The original time signal can be viewed as a sum of Fourier coefficients and their basis functions  $\{e^{ikt}\}_{k \in \mathbb{Z}}$ . In wavelet theory, there are multiple available basis functions (see Figure 3). The discrete wavelet transform is a sum of wavelet coefficients multiplied with their basis functions, which vary not in frequency but in width and location. A simple example is presented in Figure 2, where a snippet of the inversion model with 4 model parameters has been decomposed in the wavelet domain. In this example, Daubechies 1 or Haar wavelets are used. The scaling function  $\phi_{0,0}$  (or mother function) is simply a

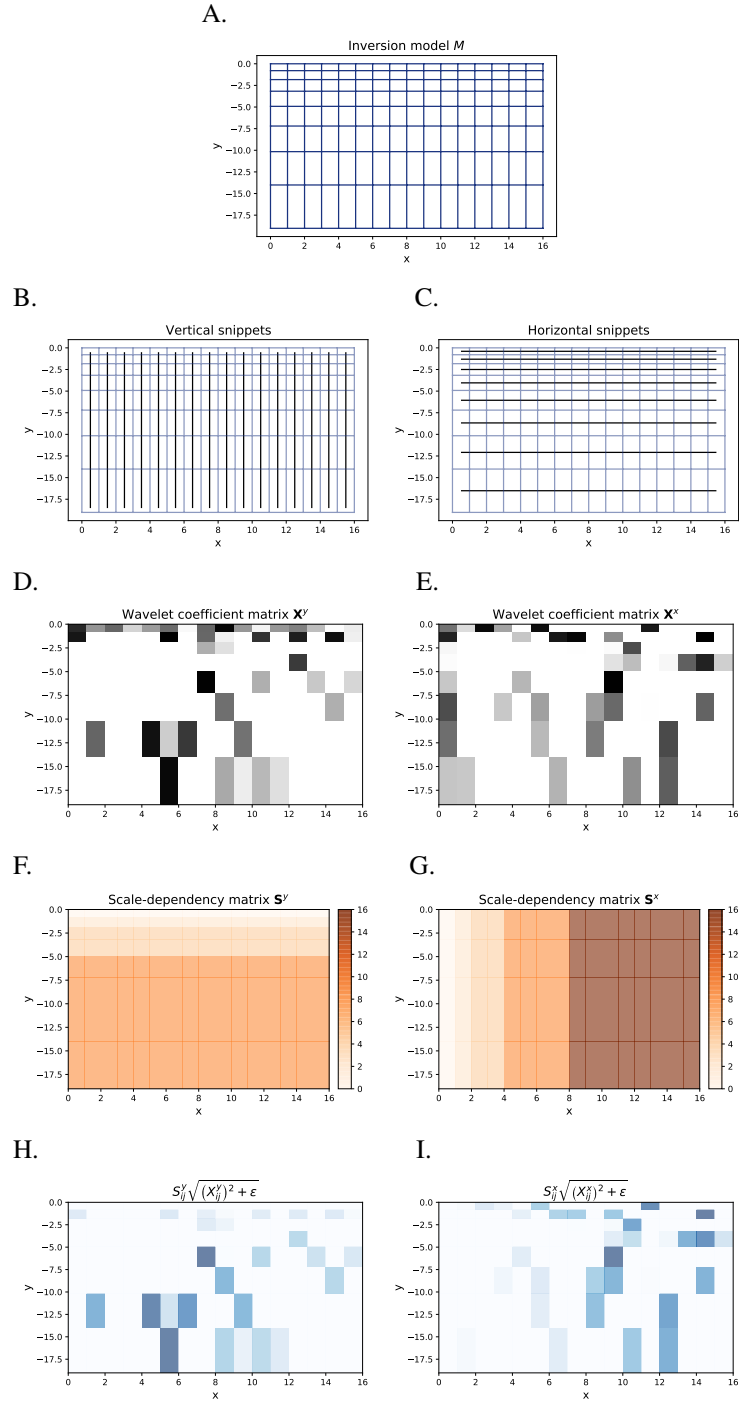


**Figure 1.** Conceptual visualization of the consecutive steps towards the scale-dependent wavelet-based model misfit. The inversion model  $M$  with a discretization (A.) is sliced in vertical and horizontal snippets (B. and C.). On each snippet, the 1D discrete wavelet transform is applied. The wavelet coefficients in D. and E., together with the scale-dependency matrices F. and G. are used in the perturbed Eklblom measure in H. and I.

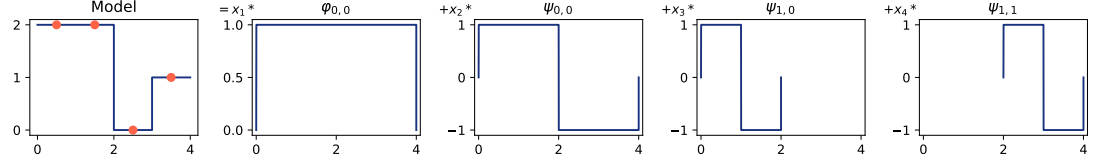


**Figure 2.** A simple example of a wavelet decomposition of a model with four model parameters into four wavelet basis functions. The model  $\mathbf{m} = 1.25\varphi_{0,0} + 0.75\psi_{0,0} + 0\psi_{1,0} + 0.5\psi_{1,1}$  (the coefficients of the true wavelet transform are rescaled with  $\sqrt{2}/2$  for each extra level, due to a scaling factor that was omitted in Eq. (4) and here for clarity).

block function over the whole domain of the model  $\mathbf{m}$ . The other wavelet functions are built from this mother function, that is a wavelet function  $\psi_{0,0}$  and two wavelet functions with smaller compact support  $\psi_{0,1}, \psi_{1,0}$ . The relations between the wavelet function are as follows:

$$\psi_{n,k}(t) \sim \psi(2^n t - k), \quad (4)$$

where  $\psi(t)$  is the wavelet basis function  $\psi_{0,0}$ . The first parameter is related to the compact support width. The lower the  $n$ , the wider the compact support width. The  $k$  parameter controls the translation. So each wavelet function gauges the model with a specific temporal and spatial resolution. One can always find wavelet-coefficients  $x_i$ , where  $i \in [1, 2, 3, 4]$ , such that the aforementioned model is exactly represented in terms of those four basis functions. When trying to find the coefficients by hand, it is evident that coefficient  $x_3$  corresponding to basis function  $\psi_{1,0}$  should be zero for this specific example. This is the foundation of the sparsifying nature of the wavelet transform. A more detailed example is found in Deleersnyder et al. (2021) or in standard works about wavelet theory, such as Mallat (1999).

The discrete wavelet transform is reliably computed via the Fast Wavelet Transform, as e.g., implemented in the PyWavelets package (Lee et al., 2006). It boils down to a matrix multiplication on each 1D snippet  $\mathbf{m}$ , which generates the wavelet representation  $\mathbf{x}$ . Repeating this on each snippet generates a matrix  $\mathbf{X}$  with wavelet representations for each orientation:

$$\mathbf{X}^x = \mathbf{W}^x \mathbf{M}, \quad \mathbf{X}^y = \mathbf{M} \mathbf{W}^{yT}, \quad (5)$$

where each orientation has its own basis transformation matrix  $\mathbf{W}^{x/y}$ . A conceptual illustration of such sparse wavelet coefficient matrices  $\mathbf{X}$  are shown in Figure 1D-1E.

### 2.2.2 Choice of the wavelet

There exist many different types of wavelet basis functions. Wavelet basis functions with similar properties are grouped in wavelet families. Those wavelets within a family are often developed to possess specific characteristics in shape but are more often the result of possessing some other mathematical properties (symmetry, orthogonality, minimal compact support...). The shape of the wavelet is often a corollary. The Haar wavelet (already used in Figure 2) is likewise a wavelet from the Daubechies family. This family is by far the best-known and will be the only family used here. The Haar wavelet is also known as the Daubechies one (db1) wavelet. The ‘one’ refers to the number of ‘vanishing moments’. This decisive property of a wavelet is defined as follows:

A wavelet has  $p$  vanishing moments when

$$\int t^k \psi(t) dt = 0 \quad \text{for } k = 0, 1, \dots, p-1. \quad (6)$$

The number of vanishing moments is related with the compact support of the wavelet: an orthonormal wavelet with  $p$  vanishing moments has at least a support of size  $2p-1$  (Daubechies, 1988). The Daubechies family is defined (by imposing mathematical properties rather than on appearance, cf. supra) as the set of wavelets with minimal compact support, given a number of vanishing moments  $p$ . All the mother wavelet basis functions that are being used in this work are listed in Figure 3.

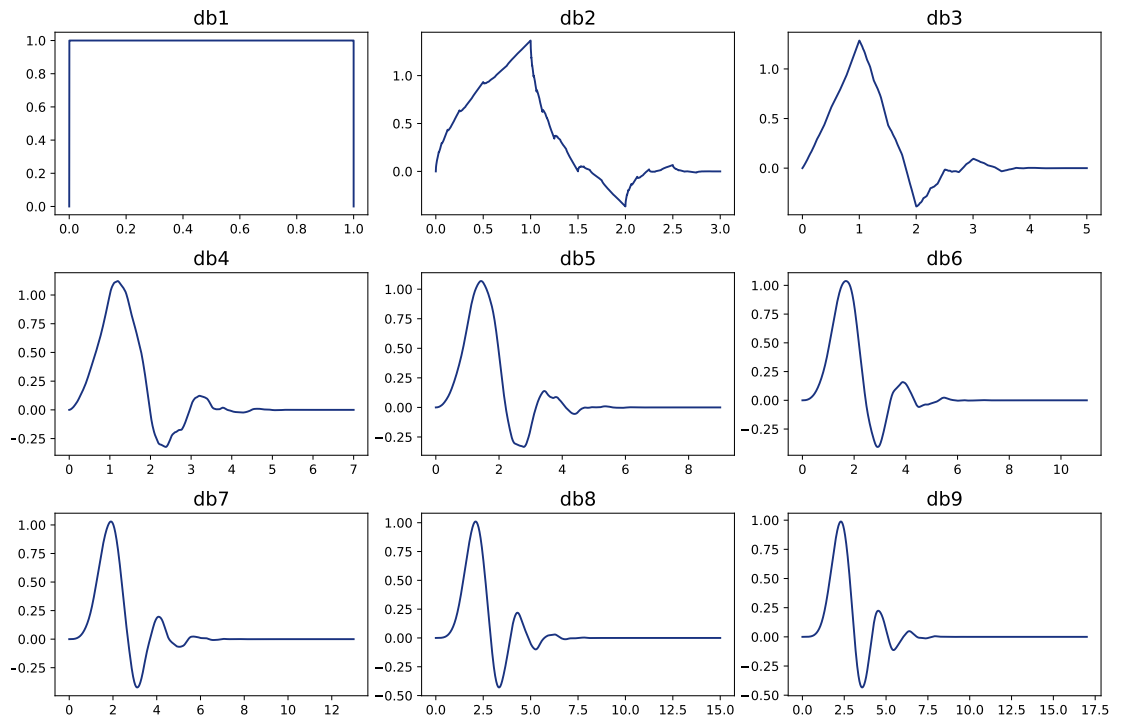


**Figure 3.** Daubechies mother wavelets  $\phi$ .

The Daubechies family is known for having good approximating abilities, this means that it can represent many piecewise smooth models in a sparse fashion (see Section 2.2.3). The number of vanishing moments also has an effect on the sparsity of an inversion model. Equation (6) implies that a wavelet with  $p$  vanishing moments is orthogonal to polynomials of degree  $p - 1$ . Hence, the db2 wavelet is orthogonal to linear functions and this guarantees that wavelet-coefficients will be zero for linear pieces in an inversion model  $\mathbf{m}$ . The greater the number of vanishing moments, the more complex structures can be represented in a sparse fashion.

It is beyond the scope of this study to examine the “optimal” choice of (multiple) basis function(s). As Oldenburg et al. (2020) argue, geoscience problems and their related algorithmic problems tend to become more complex and multidisciplinary in nature. Driven by scientific curiosity, subsurface investigations will ever-increasingly become more complex. The flexibility of the proposed inversion scheme allows for more complex inversion strategies and can produce multiple subsurface realizations that fit the data equally well, yet “simple” in Occam’s sense. It will be part of future work to define criteria for finding the best wavelet basis. For now, the geoscientist will need to trust on expert knowledge, guiding geological data, and acknowledge that the only true criterion is based on the data misfit. The ensemble of inversion models allows to reveal different features within the same framework of wavelet-based inversion.

The “best” choice for the wavelet basis function thus depends on the geological interpretation and prior knowledge. For example, when a EM borehole logging along the profile is available, it is possible to calibrate method against the sharpness seen in the vertical conductivity profile. If no prior knowledge or validation data is available, the only criterion is the data misfit or chi-squared criterion. Knowing that many solutions can yield the same data misfit, relying on an ensemble of inversion models that fit the data equally well is then at least as valid as relying on solely one inversion model from another method. A major strength of this method over conventional deterministic methods is that it can adapt the sharpness differently in both orientations by simply tuning the parameters, that is the number of vanishing moments of the wavelet basis function used in each orientation.

### 2.2.3 Scale-dependent complexity measure

The idea behind the scale-dependency can be understood with the building block metaphor. An inversion model is built with all the (compactly supported) building blocks with different widths (or dilatation parameter  $n$ ). When playing with wavelet-building blocks, there is a rule that the blocks can only be placed at specific locations, determined by the parameter  $k$ . This is a sparsity-based regularization scheme, thus one tries to build the inversion model with the least number of building blocks, or with as much vanishing wavelet coefficients as possible. Adding the scale-dependency to the scheme is basically adding the rule that for using smaller or narrower building blocks (with high dilatation parameter  $n$ ), a higher price has to be paid. This is intuitively clear because a minimum structure model is simple if it gives priority to larger structures, rather than to small details. Using multiple small building blocks usually corresponds to adding (potentially too many) details to the model. The idea of adding scale-dependency to the regularization scheme also has a theoretical origin, described in Deleersnyder et al. (2021).

We introduce specific scale-dependency matrices  $\mathbf{S}^x, \mathbf{S}^y$  which depend on the structure of the wavelet coefficient matrices  $\mathbf{X}^x, \mathbf{X}^y$ . The entries of  $\mathbf{S}$  are zero if it corresponds to coefficients of the mother wavelet or scaling function in  $\mathbf{X}$  (those coefficients determine the ‘total energy’ of the model, in other terms if the scaling coefficients are zero, the integral over the model should be zero). This is because those coefficients must never be zero for a realistic inversion model and should therefore not be minimized. Note that in the conceptual Figure 1D and 1E, all scaling function coefficients are *not* zero. The other entries of the scale-dependency matrices  $\mathbf{S}$  are  $2^n$ , where  $n$  is the dilation parameter of the corresponding entry in  $\mathbf{X}$ . The scale-dependency matrices  $\mathbf{S}^x, \mathbf{S}^y$  of our conceptual example are shown in Figures 1F and 1G.

In Deleersnyder et al. (2021), we compare our scale-dependent regularization scheme with a different wavelet-based regularization scheme without this scale-dependency feature. A main advantage is that the scale-dependency of our scheme allows the use of wavelets with few vanishing moments and is, therefore, an improvement with respect to existing wavelet-based regularization schemes which are mostly successful with wavelets with larger vanishing moments (and thus smooth models). In conclusion, the idea of scale dependency has both an intuitive and theoretical justification and has already proven to produce successful results.

### 2.2.4 The perturbed $\ell_1$ -Eklblom measure

The presented minimum-structure regularization scheme is based on sparsity. The perfect sparsity measure would be the  $\ell_0$ -‘norm’, which is in fact a quasi-norm. It counts the number of non-zero entries in a vector. However, the  $\ell_0$ -‘norm’ is impractical in optimization. Donoho (2006b) has shown that the  $\ell_1$ -norm is a good approximation for the  $\ell_0$ -‘norm’ and thus a reliable sparsity promoting measure. There is a vast amount of literature about the optimization of  $\ell_2$ - $\ell_1$  minimization schemes, where we enter the field of compressed sensing (Donoho, 2006a). In our optimization problem, measurement errors induce noise and therefore basis pursuit denoising (BPDN) is preferred (Chen and Donoho, 1994). This will solve the optimization problem faster than an exact linear program. BPDN is a quadratic convex problem and can be solved by many general solvers, such as described in Nocedal and Wright (2006). We will rely on gradient decent-like methods and delve deeper in this in Section 2.4.

The  $\ell_1$ -norm is not differentiable at zero, therefore the perturbed  $\ell_1$ -norm measure of Eklblom (Eklblom, 1987) is used. The measure

$$\mu_{\text{Eklblom}}(x) = \sqrt{x^2 + \varepsilon} \quad (7)$$

reduces to the  $\ell_1$ -norm for vanishing  $\varepsilon$  and is also convex. The latter is a welcome property for the optimization problem. In our scheme, wavelet coefficients  $x_i$  smaller than  $10^{-4}$  have little effect on the actual conductivity profile in the model domain. Further tests on the sensitivity of  $\varepsilon$  reveal that there is only a negligible effect of the value of  $\varepsilon$  on the inversion result. In this paper,  $\varepsilon$  is always set equal to  $10^{-6}$ .

In Figures 1H-1I, the model misfit, before summation, is shown. The darker, the larger the cost of the entry. Note that due to the scale dependency, the wavelet coefficients corresponding to coarser wavelet basis functions are lighter and that coefficients from the scaling functions do not contribute at all.



### 2.2.5 Calibration: Relative weighting parameter $\alpha$

In summary, the scale-dependent wavelet-based model misfit term in two dimensions is

$$\phi_m(\mathbf{M}) = \phi_{m,\uparrow}(\mathbf{M}) + \alpha\phi_{m,\leftrightarrow}(\mathbf{M}) \quad (8)$$

$$= \sum_{i,j} S_{ij}^x \sqrt{(X_{ij}^x)^2 + \varepsilon} + \alpha \sum_{i,j} S_{ij}^y \sqrt{(X_{ij}^y)^2 + \varepsilon}, \quad (9)$$

where  $X_{ij}^x = W^x M$ ,  $X_{ij}^y = W^y M^T$ , and  $\alpha$  balances the relative weight of both individual model misfit terms. With an extra calibration step, the parameter  $\alpha$  can be estimated. On the one hand, this can be the final parameter  $\tilde{\alpha}$ , or it can be chosen as the initial  $\tilde{\alpha}^0$  in a more comprehensive optimization strategy (in our examples, we demonstrate this with a sweep centered around  $\tilde{\alpha}^0$ ). If we deviate from  $\tilde{\alpha}$ , we label this with  $\gamma$ , such that

$$\alpha = \gamma\tilde{\alpha}. \quad (10)$$

For AEM data we know that early time data is sensitive to the upper layers of the inversion model and that late time data probes deeper layers. Moreover, one expects that the response increases if the electrical conductivity increases, so the raw TDEM data in itself gives an insight into the amount of structure/complexity to expect in inversion models. As an extreme case, for horizontally stratified inversion models you have no lateral variation in the (noise-free) data, while a sharp, lateral transition in the data will correspond to a sharp, lateral transition in the inversion model. We propose the following method for the estimation of  $\alpha$ .

We propose the parameter  $\tilde{\alpha}$  as the ratio of the estimation of the model misfit in the vertical orientation  $\tilde{\phi}_{m,\uparrow}$  by the model misfit of the horizontal orientation  $\tilde{\phi}_{m,\leftrightarrow}$ :

$$\tilde{\alpha} = \frac{\tilde{\phi}_{m,\uparrow}}{\tilde{\phi}_{m,\leftrightarrow}}. \quad (11)$$

$\tilde{\phi}_{m,\uparrow}$  is estimated by randomly picking a sounding and to perform a 1D inversion with the appropriate wavelet basis function (up to  $\phi_d = 1$ ). The model complexity is then extrapolated on each sounding and thus

$$\tilde{\phi}_{m,\uparrow} = n_s \cdot \phi_{m,1D}. \quad (12)$$

Clearly, this estimation can be improved by averaging over 1D model complexities of multiple soundings. In this work, only one sounding is used for the estimation of  $\tilde{\phi}_{m,\uparrow}$ . This is because the result of  $\tilde{\alpha}$  depends more on the choices of the wavelet basis functions in each orientation, rather than on the actual 1D inversion models.

For the estimation of  $\tilde{\phi}_{m,\leftrightarrow}$ , the data is multiplied with a normalization factor. For the data  $d^i$  at time channel  $i$ , the normalized data  $\tilde{d}^i$  is computed as

$$\delta^i = \frac{d^i}{\max(d^i) - \min(d^i)} \quad (13)$$

$$\tilde{d}^i = \delta^i - \min(\delta^i) + 10^{-9}, \quad (14)$$

where the  $\min(\delta^i)$  translates the negative data to positive values (the value for electrical conductivities are always positive) and  $10^{-9}$  ensures strict positiveness for the log-transform (see later). Then the lateral model misfit is computed on the data (each time channel corresponds to a horizontal snippet). This is then corrected for the total number of snippets in the inversion model, i.e., divided by the number of time channels and multiplied with the number of layers in the discretization of the sounding  $n_m$ .

We highlight that the motivation behind the calibration step is twofold: the first and most important reason is that  $\phi_{m,\uparrow}(\mathbf{M})$  and  $\phi_{m,\leftrightarrow}(\mathbf{M})$  can differ greatly, due to multiple reasons. One cause can be

that the number of soundings is much larger than the number of vertical model parameters. Another significant cause is the choice of the wavelet basis. A snippet  $\mathbf{m}$  can generate a much larger model misfit in one wavelet basis than another. Since we want to potentially generate all different wavelet-wavelet combinations, without manually picking an  $\alpha$ , this automation step is crucial. The second reason for this calibration is that, thanks to the use of complexity in the AEM data, the calibration can also estimate an (initial) value for the relative regularization parameter  $\alpha$ , ‘knowing’ about the expected lateral complexity.

### 2.3 The forward model

The forward model  $\mathcal{F}$  describes the soil’s response to a magnetic dipole, given the parameter distribution of the subsurface and the set-up of the measurement instrument. There exist two main types of forward models: (1) (semi-)analytical forward models that solve the (continuous) Maxwell equations and (2) simulations based on discretization of the physics. To mimic the full 3D soil response of the potentially non-1D subsurface, one resorts to 3D simulations of the physics. However, for geophysical inversion this is computationally intractable, primarily because of the computation of the Jacobian.

In this work, we resort to the semi-analytical solution by Hunziker et al. (2015). It derives the magnetic field response for a 1D layered earth in the wavenumber-frequency domain in a more general fashion than Wait (1951). The transformation into space and time domain is via the Hankel and Fourier transform, respectively. An open-source Python implementation by Werthmüller (2017) neatly implements those equations in a fast and reliable fashion, allowing to select between the most common Fourier and Hankel transform methods. In this paper, we have employed the digital linear filters by Key (2009) (Key 81 pt cosine sine filter and Key 201 pt Hankel filter). They are a more recent version of the digital filters behind the fast Hankel transform by Anderson (1979) and have proven to be very fast and precise for frequencies in the range of CSEM data (Werthmüller, 2017). The Jacobian is quickly obtained via finite differences, computed in parallel. The choice to use a 1D forward model recasts this regularization scheme to a quasi-2D inversion scheme.

### 2.4 The minimization scheme

There are various optimization algorithms available that are well-suited to use in conjunction with nonlinear problems. While for 1D inversion, the focus is mainly on the effect of the model misfit on the inversion model, the optimization algorithm is often a quasi-Gauss-Newton scheme and receives little attention. For 2D and 3D geophysical inverse problems, the optimization algorithm has a more substantial impact on the general performance of the inversion scheme. There are two reasons for this. First, the computation of the forward problem and its Jacobian is much more expensive. For the inversion to remain tractable, this sets a limit on the number of iterations. The optimization algorithms with the fastest (early) convergence rate are thus preferred. Secondly, the number of model parameters is typically more numerous in 2D or 3D inverse problems than for the 1D case, which is inherently more challenging.

While the optimization algorithm being essential, it is not the focus of this paper. Convergence rates of iterative methods appear to be highly problem dependent and difficult to pin down (Auken et al., 2017), while comparative studies do not tend to be general and conclusive (Haber, 2004). More specific literature for geophysical inversions, such as 3D TDEM data inversion and large-scale parameter identifications exist (Haber et al., 2007), but the adoption of those algorithms is not straightforward and the performance on our scheme unclear. The choice to rely on existing software is not only the ‘easy’ option, but also decreases the effort that other researchers have to invest to adopt the current inversion scheme. SciPy (Jones et al., 2001) stands out in terms of ease of use, both in terms of installation and implementation of the inverse problem. The L-BFGS-B method (Zhu et al., 1997) uses a FORTRAN implementation under the hood and works perfectly for our problem. It is a quasi-Newton method where the Hessian is approximated and improved at each iteration.

The inversion model will change according to the regularization parameter  $\beta$  and an optimal  $\beta$  remains to be determined. (Hansen, 2010) discusses the common automatic methods to estimate an optimal regularization parameter. More recent and sophisticated techniques exist (Valentine and Sambridge, 2018; Lima et al., 2019), but in this work we limit the methods to the most widely used criteria: the L-curve criterion and the discrepancy principle. An L-curve is a log-log plot of the data misfit term with respect to the model misfit term. This method requires to solve the inverse problem for multiple regularization

parameters and plots the model misfit in terms of the data misfit. It is expected that the outcomes of each inversion will appear in an L-shape: there will be branches in which a change in the regularization parameter will yield a significant change in either the data or model misfit. There will be a corner in which the change in the regularization parameter will yield a roughly equal significant change in both misfits. In general, there is no guarantee that the curve will exhibit an L-shape. The discrepancy principle states that the optimal regularization parameter is the one that corresponds to a data misfit  $\phi_d$  equal to the “discrepancy” in the data, i.e., the noise. With our chi-squared data-misfit, we choose the inversion model with the data-misfit closest to one. The main drawback is that this criterion depends on the estimation of the noise present in the data.

To reduce the computational burden, we adopt a warm-start strategy. Starting from a relatively high initial regularization parameter  $\beta_0$ , we sequentially run a new set of iterations with smaller regularization parameters, with the inversion model from the previous set of iterations as starting model. The beta-cooling strategy is based on heuristics. The initial regularization parameter  $\beta_0$  is determined via

$$\beta_0 = \frac{\phi_d(M^r)}{\phi_m(M^r)}, \quad (15)$$

where  $M^r$  is a randomly generated inversion model (each cell is drawn from a uniform distribution). Then, the regularization parameter  $\beta$  is cooled, depending on the number of iterations of the previous set of iterations, as few iterations suggest that the objective function has not fundamentally changed with the new cooled  $\beta$ -value. If the number of iterations of the previous is more than 50, the regularization parameter is reduced with only 10%. When the number of iterations is between 20 and 50, the regularization parameter is reduced with 25%. When the number of iterations is below 20, the regularization parameter is reduced with 40%. These cooling factors are being decided through experience. Loosening the conditions (fewer iterations, higher cooling factors) will reduce the overall computation cost, but increases the risk of overshooting the target data misfit. Adopting stricter conditions (higher number of iterations, lower cooling factors) will increase the computation time. This cooling schedule is not critical to our regularization scheme. It remains possible, yet less convenient, to restart from the set of iterations  $j + 1$  (which are stored) and redefine the cooling schedule, when appropriate.

### 3 RESULTS

In this section, we demonstrate the flexibility of our regularization scheme, that is the potential to recover blocky, smooth, and intermediate inversion models and the combination of blocky shapes in one direction and smoother transitions in the other.

We have selected a synthetic model in a similar context to our field data case of Section 3.2 such that we can use the specific conclusion to our case study. The geophysical survey has an identical set-up as the real field data case, that is time-domain AEM data obtained with a SkyTEM’s 304M system, which has a dual moment central-loop configuration. The Low Moment (LM) has a higher resolution in the shallow subsurface, because it is possible to interpret the early time channel gates. Its peak moment of approximately 3000 Am<sup>2</sup> has a sampling frequency of 325 Hz. The High Moment (HM) has a larger resolution at larger depths, due to its peak moment of approximately 100 000 Am<sup>2</sup>. The HM is sampled with a frequency of 75 Hz. Both the LM and HM have a non-square waveform (see Delsmans et al. (2019)). The LM has an on and off-time of 800 and 738  $\mu$ s respectively, while the HM has much longer on and off-times, 2500 and 4167  $\mu$ s respectively. The transmitter loop is an octagon of 340.8 m<sup>2</sup>, but this is approximated by a loop in the forward model. The receiver coil measures the  $z$ -component of the magnetic field and has an effective receiver area of 105 m<sup>2</sup>. It is located 2 m above and 13.20 m behind the centre of the loop. The height of the loop w.r.t. the surface varies with an average of 40.8 m (15.2 m std) and is measured with an altimeter. This variation is taken into account, while the tilt has been neglected. In the synthetic data case, the altitude is fixed to 40 m.

#### 3.1 Synthetic data case

The synthetic model is shown in Figure 4 and is taken from Lebbe and Pedé (1986). It is a profile from the Belgian-French border which is covered by mudflats and where the upper part is freshwater that rests

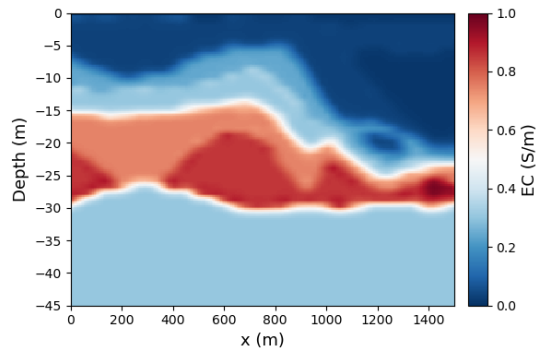


**Figure 4.** Synthetic model (adapted from Lebbe and Pede (1986)).

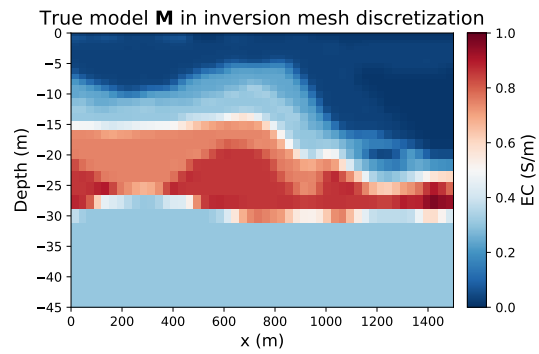


**Figure 5.** Synthetic model (adapted from Lebbe and Pede (1986)) with the discretization of the inversion model.

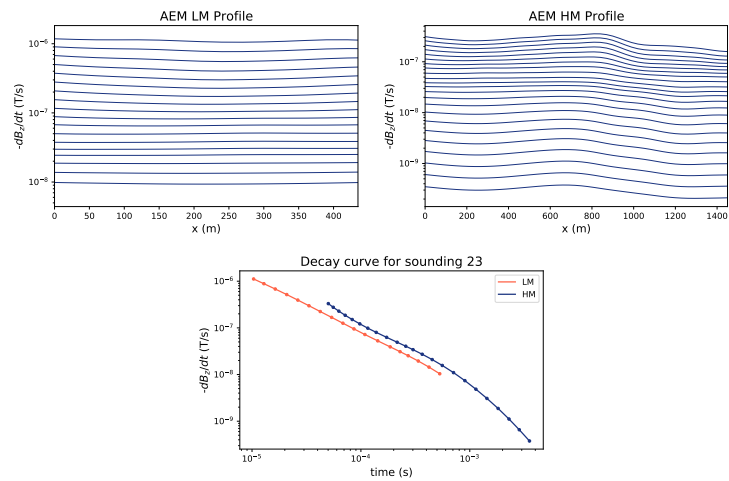


**Figure 6.** Synthetic data (see supplementary data).

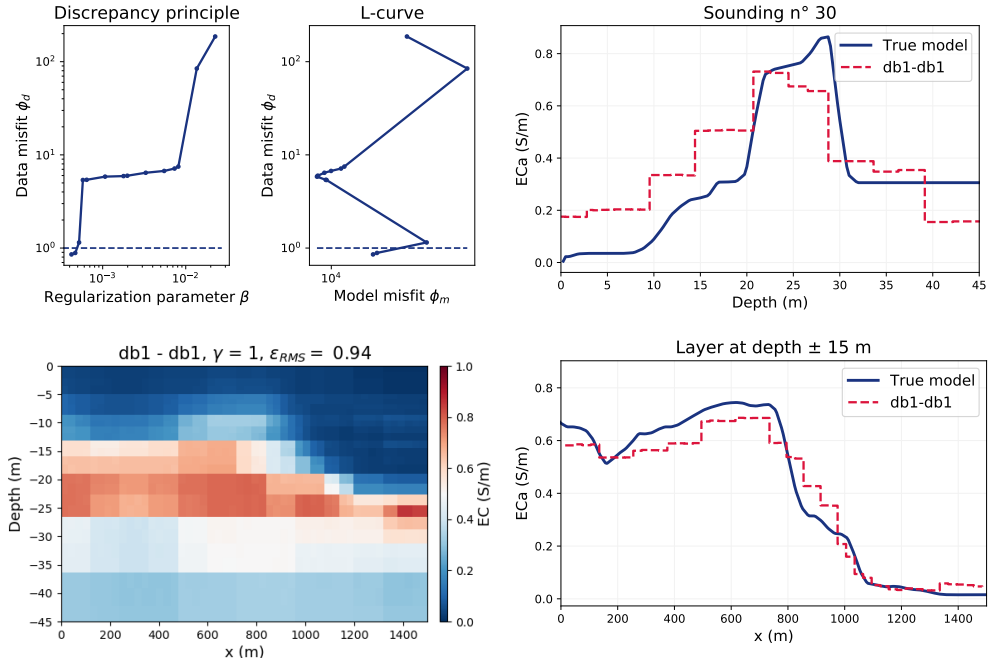


**Figure 7.** Inversion model before the  $\alpha$ -parameter calibration.

on a brackish bottom layer. The brackish water rises near two drainage ditches due to an upward flow (located at a distance  $X$  of 0 and 600 m). The first layer ends at approximately 30 m and has a mostly sandy lithology, while at 30 m depth, the Kortrijk Clay formation is reached on which the saltwater rests. The synthetic model has a large variation in model parameter values, ranging from 5 mS/m to 1000 mS/m.

The synthetic data is generated with SimPEG's finite volume method forward modelling solver (Cockett et al., 2015; Heagy et al., 2017) and the moving footprint approach (Cox et al., 2010) which allows for parallelization, such that the data contains a multidimensional component to make the synthetic data case more realistic. Note that this forward model is different for the (much faster) 1D forward model used in the inverse problem. 3% multiplicative noise is added to the synthetic data. There are 45 vertical model parameters, with equidistant spacing in  $\log_{10}$ -space, where the thicknesses range from 0.48 for the first layer and up to 7.75 meters for the lowest lying layer (note that not all the model parameters are shown).

The discrepancy between 1D and 2.5D modelling turns out to be limited and accounts for a data misfit  $\phi_d$  of 0.6 in the absence of the 3% multiplicative noise. The average relative error is  $-0.4\%$  and the standard deviation is 1.6%. When adding the 3% multiplicative noise, the data misfit  $\phi_d$  rises to 0.97, which is close to the root mean-squared error  $\epsilon_{RMS}$  equal to one, as expected. When the true model is projected on the inversion mesh (that is the discretization used in the inversion), the data misfit  $\phi_d$  rises to 1.37.

The calibration-step estimates  $\tilde{\alpha}$  and the estimates corresponding to the wavelet-wavelet combinations in Figure 9 are tabulated in Table 1. Not all wavelet-wavelet combinations are presented, we focus on inversion models with significant distinct features. There is quite some variability in  $\tilde{\alpha}$  and this relaxes the need for an extensive optimization in  $\alpha$ .

After the relative regularization parameter calibration, it is time to inspect an inversion model, generated for  $\gamma = 1$ . It is generally sufficient to check if the  $\gamma$  is 'optimal' (e.g., with geological expertise) for one wavelet-wavelet realization, which is a good characteristic of the method, given the high computational cost. In this example, the inspection is conducted with both the db1 wavelet in the vertical and lateral orientation. The result is shown in Figure 7. To select the optimal regularization parameter  $\beta$ , the L-curve turns out not to be very useful. It is not convex and therefore problematic to interpret. The L-curve criterion

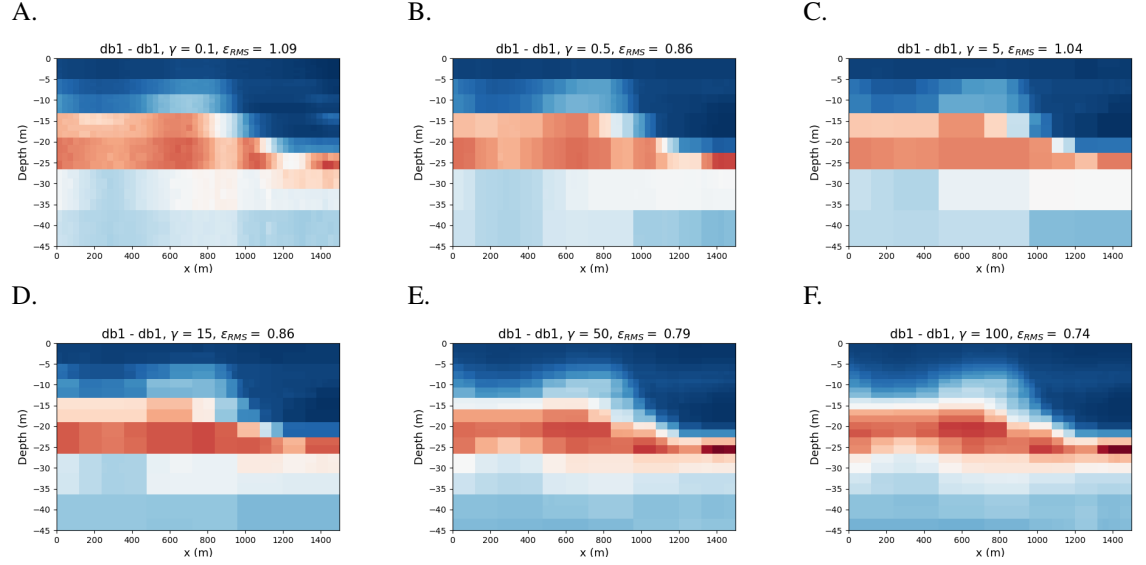


**Figure 8.** Inversion models for db1-db1, with variations over the user-defined  $\gamma$ -parameter.

as a parameter selection tool is therefore abandoned. In the discrepancy principle, we observe a relatively large hop for the data misfit. Moving from regularization parameter  $\beta = 5.7 \times 10^{-4}$  to  $\beta = 5.1 \times 10^{-4}$ , the data misfit hops from 5.37 to 1.14, and from 1.14 to 0.88 ( $= \epsilon_{\text{RMS}}^2$ ) with  $\beta = 4.6 \times 10^{-4}$ . We select the optimal regularization parameter  $\beta$  closest to  $\epsilon_{\text{RMS}}$  equal to one (and thus  $\beta = 4.6 \times 10^{-4}$ ). In this case, this is  $\epsilon_{\text{RMS}} = 0.94$ , which is slightly overfitted. The inversion model in Figure 7 nicely demonstrates the blocky structure, as expected from the db1-db1 combination. We check if  $\alpha$  is a proper choice by checking the parameter  $\gamma$ . With  $\gamma = 1$ , there are significant variations in both directions, yet it may seem that there is too much variation in the lateral direction, given that db1 wavelets tend to generate blocky models. This observation is always made within a context of prior knowledge and subject to bias. The variation is more visible in the profiles. For example, for sounding number 30 in Figure 7, the typical blocky structure is prominent, as expected from an 1D regularization scheme with a good candidate for regularization parameter  $\beta$ . For the lateral variation, for example at a depth of  $\pm 15$  m, the inversion model agrees with the true model. The issue here is that this inversion model does not exhibit the minimum structure, as we would expect from a blocky inversion. The transitions are relatively smooth and thus costly (in terms of lateral model misfit  $\phi_{m,\leftrightarrow}$ ). Increasing the relative cost of the lateral model misfit functional or thus  $\alpha$  would overcome this issue. This is done manually by setting the  $\gamma$ -parameter. It may also be expected that if the total model misfit rises, the data misfit also rises and will lie closer to one. Put differently, the overfitting leading to a data misfit smaller than one may be a result of overfitting in the lateral orientation.

In the case of a suboptimal  $\gamma = 1$  inversion model, a sweep over  $\gamma$  is warranted. An example of a sweep is shown in Figure 8, where the inversion models for  $\gamma = 0.1, 0.5, 5, 15, 50$  and  $100$  are shown (for  $\gamma = 1$ , refer back to Figure 7). It is important not to focus on a specific profile, but to look at the whole 2D inversion model. For  $\gamma = 0.1$  for example, at first sight, a minimum-structure block from  $-13$  to  $-27$  m depth and  $0$  to approx.  $800$  m in the lateral orientation is observed. However, there is quite some heterogeneity in that block that is a result of overfitting. For  $\gamma = 100$ , we observe excessive minimal structure in the lateral orientation, seen as elongated building blocks. The  $\gamma = 5$  inversion model seems to be a good candidate as it seems to be less overfitted than the  $\gamma = 1$  inversion model. Its data misfit is 1.04, which is close to one and the inversion model itself is blocky in both vertical and lateral directions. Note that prior knowledge may let the geoscientist make another decision, but we conclude that  $\gamma = 5$  is optimal. Note that this is not far from  $\gamma = 1$ , which means that strategy was at least a good starting point.

Once the user-defined  $\gamma$ -parameter has been picked, the manifold of the inverse problems can be constructed, where all the potential interesting combinations of the wavelet basis functions can be used.

Wavelet combination	$\tilde{\alpha}$
db1-db1	0,500
db1-db2	2,82
db1-db5	58,1
db2-db3	0,750
db3-db2	0,0450
db3-db8	5,45
db5-db1	0,00721
db6-db5	0,069
db6-db9	0,600
db1-db1	0,5

**Table 1.** Estimated parameter  $\tilde{\alpha}$  for each wavelet-wavelet basis function combination in Figure 9.

The strength of the method is that both in the vertical and lateral orientation can be varied, e.g, sharp transitions and smooth transitions in the vertical and lateral orientation, respectively. Not all combinations are shown in this text because some subsurface realizations are similar. For each inversion model, the user-defined  $\gamma$  is constant and the  $\tilde{\alpha}$  is presented in Table 1.

In Figures 9A-C, the inversion models with db1 in the vertical orientation are shown. Figure 9B has larger amplitudes than Figure 9A and sharp transitions in the lateral orientation. Figure 9C also has larger amplitudes, but the lateral transitions are even smoother. The  $\epsilon_{\text{RMS}}$  is rather low, but the inversion model with a slightly larger regularization parameter  $\beta$  is severely under fitted and lies further from  $\epsilon_{\text{RMS}}$  equal to one. An alternative for the under fitted inversion model would be to look at inversion models with similar properties, such as db1-db6, as they potentially have an inversion model with a root-mean-squared error  $\epsilon_{\text{RMS}}$  closer to one. However, db1-dbn inversion models turn out to be prone to local minima (something that is infrequently observed with other combinations). Starting from db1-db3 onwards, this issue is persistent for this synthetic case, e.g., for db1-db6 the lowest  $\epsilon_{\text{RMS}}$  obtained is 7.2. The first solution would be to start from another random inversion model until an acceptable  $\epsilon_{\text{RMS}}$  after convergence is obtained, though this did not resolve this issue. Another solution is to use the db3-db5 outcome as starting model for db1-db5. This will sharpen the transitions of the inversion model along the vertical orientation, while still fitting the data. Figure 9A proves that our regularization scheme can recover blocky structures (which is an appealing feature in other cases), however, our synthetic model is not that blocky and thus this inversion model is not expected. The db6-db9 inversion model in Figure 9I is the other limiting case and is comparable with smoothing regularization. The problem with smoothness regularization is that the minimal and maximal electrical conductivity values tend to be over- and underestimated, respectively. Here, this is also the case, see for example Figure 9I. All other inversion models exhibit intermediate results, e.g., db2-db3 can recover a large peak in the vertical orientation. The db3-db2 inversion model, on the other hand, which has an identical data misfit, generates a smoother peak (see Figure 10E), which is for this inversion model more favourable. If the geoscientist rather picks one inversion model as the actual inversion model, rather than to interpret the ensemble of inversion models, it has to resort to prior knowledge. Nearby borehole loggings would for example be ideal to evaluate the sharpness in the vertical orientation. In our synthetic data case within the saltwater intrusion context, we know that the transition from fresh to saltwater is sharp, but not blocky. For example, db3 exhibits this feature. In the lateral orientation, however, relatively smooth profiles are expected. Thus db3-db8 in Figures 9F and 10C, E, F which also fits the data quite well ( $\epsilon_{\text{RMS}} = 0.96$ ) would be a good candidate. It can both recover the electrical conductivities and the global structure of the inversion model quite well, such as the rather subtle saltwater lens at 1000 m. (Note that a finer discretization (which comes with a higher computational cost) would yield better estimations of the peaks in Figure 10.)

### 3.2 Field data case

In this section, we apply the flexible quasi-2D wavelet-based inversion scheme on the airborne data of Belgian's current salinization map of vulnerable regions in Flanders (Delsmans et al., 2019). The salinization map shows the interface between salt and freshwater and serves as decision tool for policymakers to assess local measures to increase freshwater availability, which may be hindered by future effects of climate change. The use of quasi-2D inversion is justified, as the distance between the soundings along

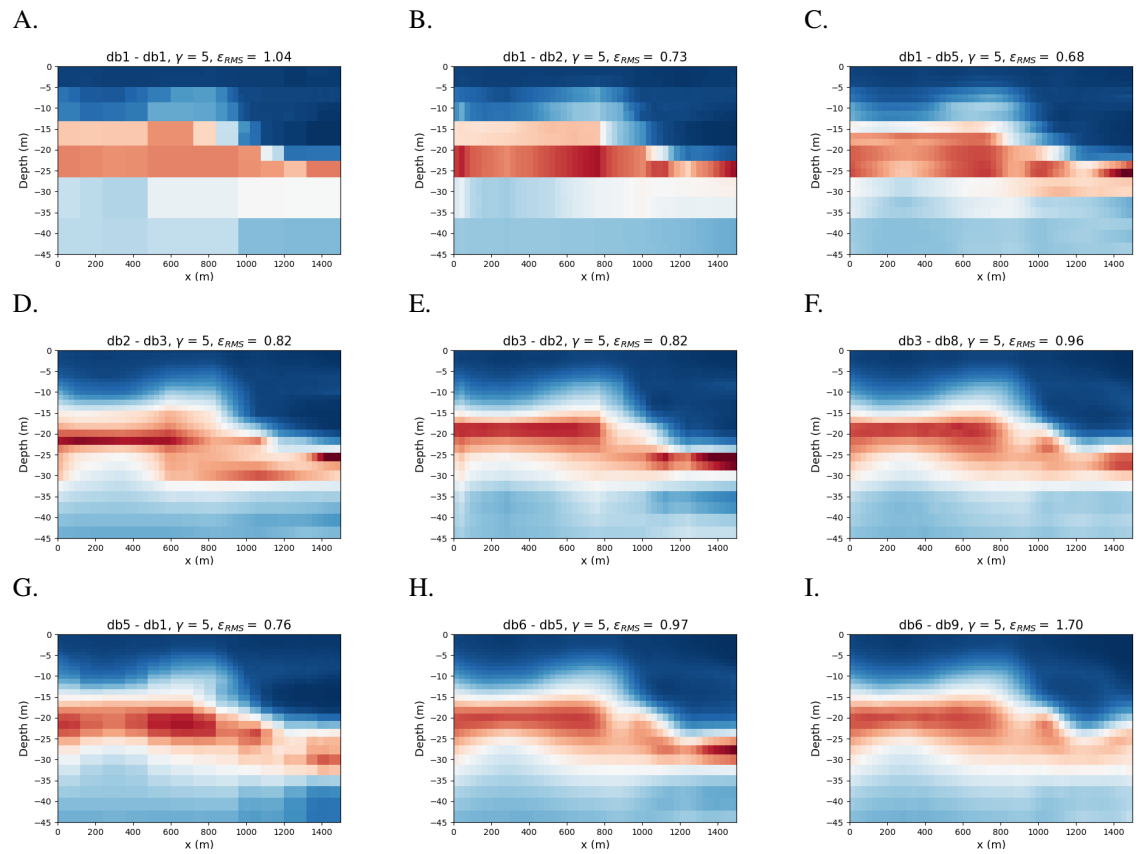


**Figure 9.** Selected models form the ensemble of inversion models.



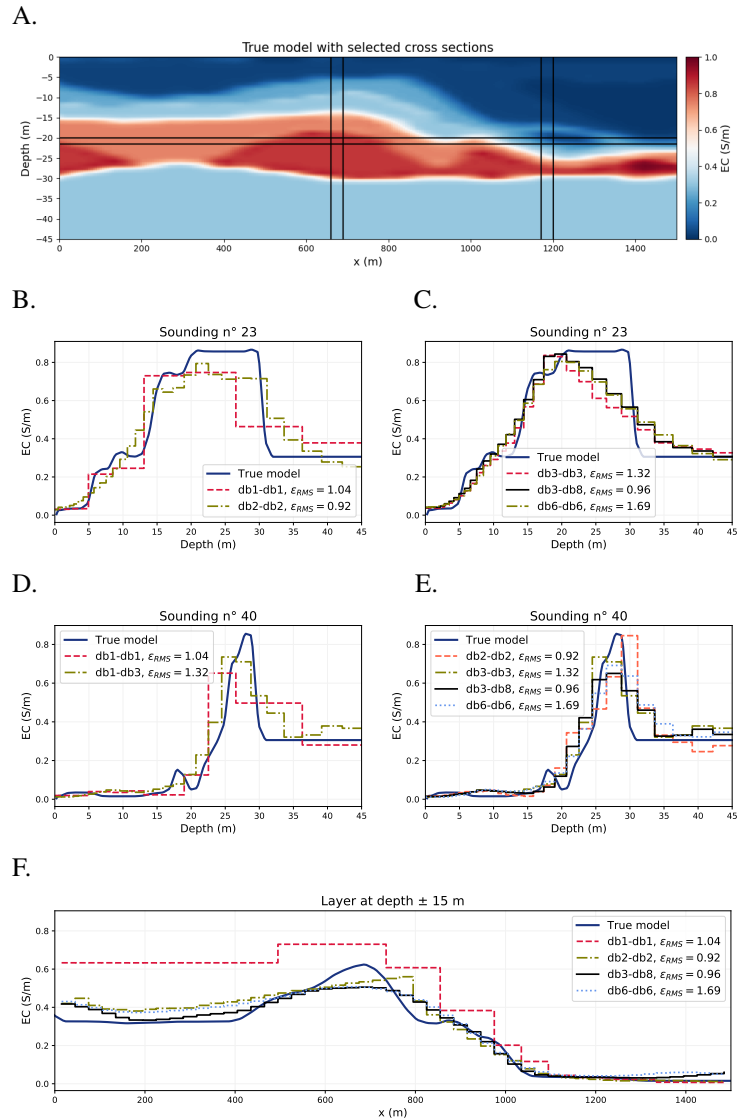


**Figure 10.** Selected conductivity profiles (synthetic model).

the line of flight is approximately 30 m, while much larger between the line of flights (between 250-275m).

We can compare our inversion models with the results of the actual salinization map. The inversion is carried out with the Aarhus Workbench software and thus uses Spatially Constrained Inversion (SCI) (Viezzoli et al., 2008). It is a quasi-3D smooth inversion, where Delaunay triangulation is used to model spatial connections between the sounding locations, or 'spatial complexity'. That spatial complexity is then minimized, as part of an objective function with standard data misfit.

To demonstrate the applicability of this method for inversion of field data, we perform an inversion on a flight line from Flanders' salinization map TDEM sub dataset with 300 soundings. The data were acquired using a SkyTEM system, as described in Section 3, in 2017 as part of the Topsoil project (Delsmans et al., 2019). The flight line crosses the Yzercreek, where creek ridge deposits occur which can be locally thick. Zeuwts (1991) reports a thick freshwater lens (TDS < 1000 mg/l), while other creek ridge deposits are thinner. At some locations, solely brackish and saline groundwater can be found under soil consisting of a thin cover of heavy clay resting on peat and lying between higher creek ridge soils.

The optimal  $\gamma$ -parameter was picked using the same method as in the synthetic data case based on the db1-db1 plot. The optimal  $\gamma$ -parameter was set to 25. The optimal regularization parameter  $\beta$  was again determined via the warm-start strategy and the discrepancy principle. All inversion models with each wavelet-wavelet combination were generated. However, we use the conclusion from the synthetic field case, which is similar to this setting, that db3-db8 is a good choice for the wavelet basis functions. We present the inversion model in Figure 11B with an  $\epsilon_{RMS}$  of 1.07. For completeness, the inversion model of the current salinization map is also shown. This was presented in Delsmans et al. (2019) and uses the same data and error estimates, but uses Spatially Constrained Inversion (SCI). The discretization in the horizontal orientation is identical (one cell per sounding), while in the vertical orientation a different discretization was applied, identical to the synthetic field case from the previous section. By doing so, we can more safely rely on the db3 as a good choice for the vertical orientation wavelet basis function.

We recognize similar trends between the two inversion models, however, the inversion model from our method provides a higher resolution image (which can be partially explained due to the finer discretization). In addition, artefacts are also recognized, such as at 625 meters. This is a property of wavelet-based inversion that was found in earlier work, where we have found that wavelet-based inversion can recover high amplitude anomalies in globally smooth profiles. Also between 3000 and 5000 m, high bulk conductivities in the shallow subsurface are found, this is much less recognized in the inversion model of SCI. The freshwater lens between 1800 and 3000 is well identified in more detail and with more realistic transitions in both orientations. In particular, the blockiness in the SCI fresh-saltwater interface in the lateral orientation is not realistic. The blockiness in the vertical orientation is possibly a result of the discretization.

The peaks in the conductivity profiles in Figure 11C are not exactly at the same depths. Sounding n° 125 shows the largest discrepancy in the peaks, which may be accounted to the fact that SCI does not recover the V-shaped fresh-saltwater interface and n° 125 right at the deepest point of the interface. Note that all conductivity profiles span larger electrical conductivity ranges than the SCI inversion model, which is smoothness-based and tends to overestimate low EC-values and underestimate high EC-values. This impacts the interpretation in terms of depth of the interface, based on a threshold on the EC-values.

We can also plot all the soundings of the acceptable inversion models on the same figure (that is an inversion model converged to at least  $\epsilon_{RMS} < 1.2$ ). These are the fine black lines in Figure 11C. Viewing the results as an ensemble gives us an idea of the non-unicity or the range of acceptable EC-values and their variability. For sounding n° 100, we observe quite some variability in the sharpness that is in agreement with the data. Smoother transitions than the db3 inversion result start from an EC-value greater than 0.1 S/m. At approximately 4 m depth, the blocky transition is identified. At 12-15 m, some models indicate that the EC-value is slightly larger than the SCI or db3-db8 inversion result. For sounding n° 125, the first 2 meters seem to be uncertain, yet the results indicate that the EC-value should be smaller than the SCI inversion result. Interestingly, the variation in the inversion results varies throughout the soundings. Sounding n° 250 does not indicate much variability in the ensemble (except for the db1-jump

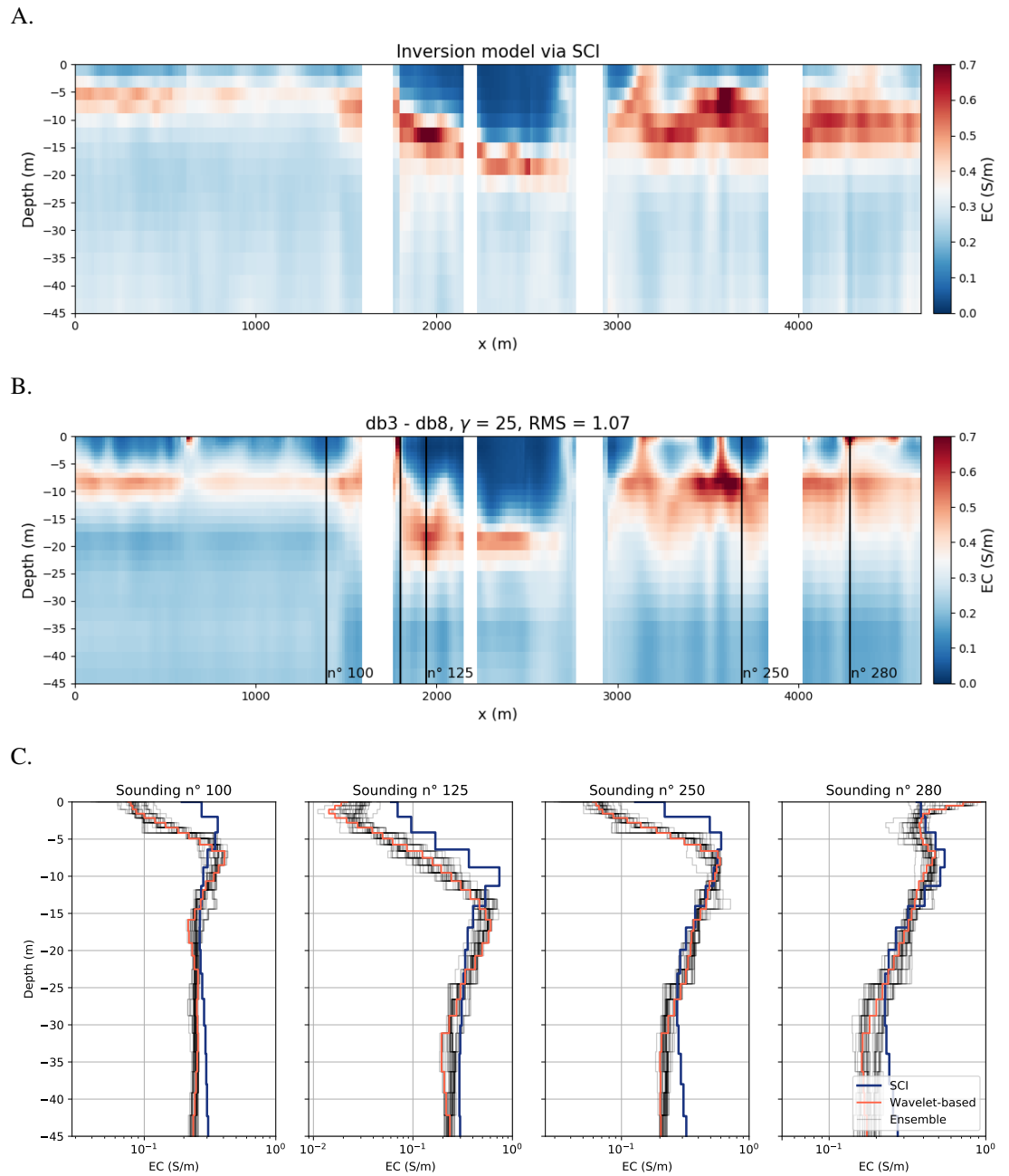


**Figure 11.** A. Inversion model of the Yzercreek profile with Spatially Constrained Inversion (SCI), by Delsmans et al. (2019). B. Inversion model with wavelet-based regularization. C. Comparison of conductivity profiles between the two inversion models.

at approximately 4 m and a small peak in EC between 12-15 m) while sounding n° 280 reveals more variation in the first few meters and at larger depths. The variation at larger depths can be explained by a reduced sensitivity due to the 'shielding' of the highly conductive artefact right below the surface. The variation right below the surface is an indication of the non-uniqueness of the inverse problem.

## 4 CONCLUSION

The multidimensional, scale-dependent wavelet-based inversion scheme is an alternative scheme that is more flexible than smoothness or blocky inversion and can easily be combined with existing frameworks of deterministic inversion (gradient-based optimization methods, L-curve criterion for optimal regularization parameter). It can recover inversion models with tunable sharpness and limiting cases (smoothness and blocky inversion). The regularization term uses the wavelet transform of an inversion model in combination with the Eklblom measure to estimate the complexity of an inversion model in Occam's sense. The choice of the wavelet basis function underlying the wavelet transform allows for defining the features in the final inversion model.

Our approach is different from other wavelet-based regularization schemes, as this regularization method allows for choosing a different wavelet basis function for each orientation and therefore, for example, obtaining sharp results along with the vertical orientation and smoother results along with the lateral orientation, which is a desirable feature for many applications, such as in a salinization context. The difficulty of pinning down the relative regularization parameter (vertical vs. horizontal complexity) is resolved with a calibration step, which uses the variability in the EM data and the complexity of one (or more) random sounding(s). We have shown that the calibration step is at least a good starting point for the optimization of that relative regularization parameter. The user is free to try to optimize that parameter if desired.

Depending on the availability of prior knowledge, different interpretation approaches can be used. If no prior knowledge is available, the high flexibility of the method can be exploited to easily generate a set of representations of the inverse problem, each highlighting different features, while fitting the data. Common features in the set of inversion models are an indication that the feature is in the geophysical data. When borehole loggings are available, the profile could be correlated with the colocated data to calibrate the sharpness along with the vertical orientation. In our example, we have used an existing profile to generate synthetic data similarly to our real field data. By analysing the ensemble of inversion models and comparing it to the original profile, we have determined that the db3 wavelet (relatively sharp) along the vertical orientation with the db8 wavelet (smooth) along the lateral orientation is a suitable candidate for the field data inversion.

We have demonstrated the potential of the flexible regularization for airborne time-domain EM data, where a different and appropriate sharpness was used in each orientation. However, the method could be equally applied to any other geophysical method. It can be straightforwardly extended to quasi-3D inversion or it can be used with full 2.5D or 3D forward models.

## ACKNOWLEDGMENTS

The authors thank VMM (Flanders Environment Agency) for making the data behind Flanders' salinization map available. The research leading to these results has received funding from FWO (Fund for Scientific Research, Flanders, grant 1113020N) and the Flemish Institute for the Sea (VLIZ) Brilliant Marine Research Idea 2022. The resources and services used in this work were provided by the VSC (Flemish Supercomputer Center), funded by the Research Foundation - Flanders (FWO) and the Flemish Government.

## DATA AVAILABILITY

The 2.5D forward data from the synthetic data case are provided in the supplementary materials. The field data that support the findings of the field data case are available from the corresponding author, Wouter Deleersnyder, upon reasonable request.

## REFERENCES

- Anderson, W. L. (1979). Numerical integration of related hankel transforms of orders 0 and 1 by adaptive digital filtering. *Geophysics*, 44(7):1287–1305.
- Auken, E., Boesen, T., and Christiansen, A. V. (2017). A review of airborne electromagnetic methods with focus on geotechnical and hydrological applications from 2007 to 2017. *Advances in Geophysics*, 58:47–93.
- Auken, E. and Christiansen, A. V. (2004). Layered and laterally constrained 2d inversion of resistivity data. *Geophysics*, 69(3):752–761.
- Chen, S. and Donoho, D. (1994). Basis pursuit. In *Proceedings of 1994 28th Asilomar Conference on Signals, Systems and Computers*, volume 1, pages 41–44. IEEE.
- Christensen, N. B. (2016). Strictly horizontal lateral parameter correlation for 1d inverse modelling of large datasets. *Near Surface Geophysics*, 14(5):403–412.
- Cockett, R., Kang, S., Heagy, L. J., Pidlisecky, A., and Oldenburg, D. W. (2015). SimPEG: An open source framework for simulation and gradient based parameter estimation in geophysical applications. *Computers & Geosciences*, 85:142–154.
- Constable, S. C., Parker, R. L., and Constable, C. G. (1987). Occam’s inversion: A practical algorithm for generating smooth models from electromagnetic sounding data. *Geophysics*, 52(3):289–300.
- Cox, L. H., Wilson, G. A., and Zhdanov, M. S. (2010). 3d inversion of airborne electromagnetic data using a moving footprint. *Exploration Geophysics*, 41(4):250–259.
- Daubechies, I. (1988). Orthonormal bases of compactly supported wavelets. *Communications on pure and applied mathematics*, 41(7):909–996.
- Daubechies, I., Defrise, M., and De Mol, C. (2004). An iterative thresholding algorithm for linear inverse problems with a sparsity constraint. *Communications on Pure and Applied Mathematics: A Journal Issued by the Courant Institute of Mathematical Sciences*, 57(11):1413–1457.
- Deleersnyder, W., Maveau, B., Hermans, T., and Dudal, D. (2021). Inversion of electromagnetic induction data using a novel wavelet-based and scale-dependent regularization term. *Geophysical Journal International*, 226(3):1715–1729.
- Delsmans, J., van Baaren, E., Vermaas, T., Karaoulis, M., Bootsma, H., de Louw, P., Pauw, P., Oude Essink, G., Dabekaussen, W., Van Camp, M., Walraevens, K., Vandenbohede, A., Teilmann, R., and Thofte, S. (2019). Topsoil airborne em kartering van zoet en zout grondwater in vlaanderen. Technical report, VMM.
- Donoho, D. L. (2006a). Compressed sensing. *IEEE Transactions on information theory*, 52(4):1289–1306.
- Donoho, D. L. (2006b). For most large underdetermined systems of linear equations the minimal  $\ell_1$ -norm solution is also the sparsest solution. *Communications on Pure and Applied Mathematics: A Journal Issued by the Courant Institute of Mathematical Sciences*, 59(6):797–829.
- Eklblom, H. (1987). The  $\ell_1$ -estimate as limiting case of an  $\ell_p$ -or huber-estimate. In *Statistical data analysis based on the  $\ell_1$ -norm and related methods: 31/08/1987-04/09/1987*, pages 109–116. Elsevier.
- Farquharson, C. G. (2007). Constructing piecewise-constant models in multidimensional minimum-structure inversions. *Geophysics*, 73(1):K1–K9.
- Goebel, M., Knight, R., and Halkjær, M. (2019). Mapping saltwater intrusion with an airborne electromagnetic method in the offshore coastal environment, monterey bay, california. *Journal of Hydrology: Regional Studies*, 23:100602.
- Guillemoteau, J., Simon, F.-X., Lück, E., and Tronicke, J. (2016). 1d sequential inversion of portable multi-configuration electromagnetic induction data. *Near Surface Geophysics*, 14(5):423–432.
- Haber, E. (2004). Quasi-newton methods for large-scale electromagnetic inverse problems. *Inverse problems*, 21(1):305.
- Haber, E., Oldenburg, D. W., and Shekhtman, R. (2007). Inversion of time domain three-dimensional electromagnetic data. *Geophysical Journal International*, 171(2):550–564.
- Hansen, P. C. (2010). *Discrete inverse problems: insight and algorithms*, volume 7. Siam.
- Heagy, L. J., Cockett, R., Kang, S., Rosenkjaer, G. K., and Oldenburg, D. W. (2017). A framework for simulation and inversion in electromagnetics. *Computers & Geosciences*, 107:1–19.
- Hermans, T., Vandenbohede, A., Lebbe, L., Martin, R., Kemna, A., Beaujean, J., and Nguyen, F. (2012). Imaging artificial salt water infiltration using electrical resistivity tomography constrained by geostatistical data. *Journal of Hydrology*, 438:168–180.
- Hunziker, J., Thorbecke, J., and Slob, E. (2015). The electromagnetic response in a layered vertical

- transverse isotropic medium: A new look at an old problem. *Geophysics*, 80(1):F1–F18.
- Jones, E., Oliphant, T., Peterson, P., et al. (2001). SciPy: Open source scientific tools for Python. [Online; accessed 12-01-2019].
- Kemna, A. (2000). *Tomographic inversion of complex resistivity: Theory and application*. Der Andere Verlag.
- Key, K. (2009). 1d inversion of multicomponent, multifrequency marine csem data: Methodology and synthetic studies for resolving thin resistive layers. *Geophysics*, 74(2):F9–F20.
- Klose, T., Guillemoteau, J., Vignoli, G., and Tronicke, J. (2022). Laterally constrained inversion (lci) of multi-configuration emi data with tunable sharpness. *Journal of Applied Geophysics*, 196:104519.
- LaBrecque, D. J., Miletto, M., Daily, W., Ramirez, A., and Owen, E. (1996). The effects of noise on occam's inversion of resistivity tomography data. *Geophysics*, 61(2):538–548.
- Lebbe, L. and Pede, K. (1986). Salt-fresh water flow underneath old dunes and low polders influenced by pumpage and drainage in the western belgian coastal plain. In *Salt water intrusion meeting. 9*, pages 199–220.
- Lee, G., Wasilewski, F., Gommers, R., Wohlfahrt, K., O'Leary, A., and Nahrstaedt, H. (2006). Pywavelets—wavelet transforms in python.
- Lima, W. A., Silva, J. B., Santos, D. F., and Costa, J. C. (2019). A robust interactive estimation of the regularization parameter. *Geophysics*, 84(3):IM19–IM33.
- Linde, N., Renard, P., Mukerji, T., and Caers, J. (2015). Geological realism in hydrogeological and geophysical inverse modeling: A review. *Advances in Water Resources*, 86:86–101.
- Liu, Y., Farquharson, C. G., Yin, C., and Baranwal, V. C. (2017). Wavelet-based 3-d inversion for frequency-domain airborne em data. *Geophysical Journal International*, 213(1):1–15.
- Macnae, J. and Milkereit, B. (2007). Developments in broadband airborne electromagnetics in the past decade. In *Proceedings of Exploration*, volume 7, pages 387–398.
- Mallat, S. (1999). *A wavelet tour of signal processing*. Elsevier.
- Mikucki, J. A., Auken, E., Tulaczyk, S., Virginia, R., Schamper, C., Sørensen, K., Doran, P., Dugan, H., and Foley, N. (2015). Deep groundwater and potential subsurface habitats beneath an antarctic dry valley. *Nature communications*, 6(1):1–9.
- Nittinger, C. and Becken, M. (2018). Compressive sensing approach for two-dimensional magnetotelluric inversion using wavelet dictionaries. *Geophysical Prospecting*, 66(4):664–672.
- Nittinger, C. G. and Becken, M. (2016). Inversion of magnetotelluric data in a sparse model domain. *Geophysical Journal International*, 206(2):1398–1409.
- Nocedal, J. and Wright, S. (2006). *Numerical optimization*. Springer Science & Business Media.
- Oldenburg, D. W., Heagy, L. J., Kang, S., and Cockett, R. (2020). 3d electromagnetic modelling and inversion: a case for open source. *Exploration Geophysics*, 51(1):25–37.
- Paasche, H. and Tronicke, J. (2007). Cooperative inversion of 2d geophysical data sets: A zonal approach based on fuzzy c-means cluster analysis. *Geophysics*, 72(3):A35–A39.
- Pfaffhuber, A. A., Lysdahl, A. O., Sørmo, E., Skurdal, G. H., Thomassen, T., Anschütz, H., and Scheibz, J. (2017). Delineating hazardous material without touching—aem mapping of norwegian alum shale. *First Break*, 35(8).
- Podgorski, J. E., Auken, E., Schamper, C., Vest Christiansen, A., Kalscheuer, T., and Green, A. G. (2013). Processing and inversion of commercial helicopter time-domain electromagnetic data for environmental assessments and geologic and hydrologic mapping. *Geophysics*, 78(4):E149–E159.
- Siemon, B., van Baaren, E., Dabekaussen, W., Delsman, J., Dubelaar, W., Karaoulis, M., and Steuer, A. (2019). Automatic identification of fresh–saline groundwater interfaces from airborne electromagnetic data in zeeland, the netherlands. *Near Surface Geophysics*, 17(1):3–25.
- Su, Y., Yin, C., Liu, Y., Ren, X., Zhang, B., Qiu, C., Xiong, B., and Baranwal, V. C. (2021). Sparse-promoting 3-d airborne electromagnetic inversion based on shearlet transform. *IEEE Transactions on Geoscience and Remote Sensing*.
- Thibaut, R., Kremer, T., Royen, A., Ngun, B. K., Nguyen, F., and Hermans, T. (2021). A new workflow to incorporate prior information in minimum gradient support (mgs) inversion of electrical resistivity and induced polarization data. *Journal of Applied Geophysics*, 187:104286.
- Tikhonov, A. N. (1943). On the stability of inverse problems. In *Dokl. Akad. Nauk SSSR*, volume 39, pages 195–198.
- Valentine, A. P. and Sambridge, M. (2018). Optimal regularization for a class of linear inverse problem.

- Geophysical Journal International*, 215(2):1003–1021.
- Viezzoli, A., Christiansen, A. V., Auken, E., and Sørensen, K. (2008). Quasi-3d modeling of airborne TEM data by spatially constrained inversion. *Geophysics*, 73(3):F105–F113.
- Vignoli, G., Fiandaca, G., Christiansen, A. V., Kirkegaard, C., and Auken, E. (2015). Sharp spatially constrained inversion with applications to transient electromagnetic data. *Geophysical Prospecting*, 63(1):243–255.
- Wait, J. R. (1951). The magnetic dipole over the horizontally stratified earth. *Canadian Journal of Physics*, 29(6):577–592.
- Werthmüller, D. (2017). An open-source full 3d electromagnetic modeler for 1d VTI media in python: empymod. *GEOPHYSICS*, 82(6):WB9–WB19.
- Zeuwts, L. (1991). Hydrogeologie en hydrochemie van de ijzervlakte tussen de frans-belgische grens en avekapelle-pervijze (westelijke kustvlakte). *Doctoraatsproefschrift, Universiteit Gent. Boorbeschrijving: 0, 00-0, 25:25-0*.
- Zhu, C., Byrd, R. H., Lu, P., and Nocedal, J. (1997). Algorithm 778: L-bfgs-b: Fortran subroutines for large-scale bound-constrained optimization. *ACM Transactions on Mathematical Software (TOMS)*, 23(4):550–560.